Journal of Alloys and Compounds 509 (2011) 3032–3037

Contents lists available at ScienceDirect

Journal of Alloys and Compounds

journal homepage: www.elsevier.com/locate/jallcom

Enhanced mid-IR emission in Yb^{3+}–Tm^{3+} co-doped oxyfluoride glass ceramics

Junhua Xie[a], Qiang Zhang[b,c], Yixi Zhuang[a], Xiaofeng Liu[b,c], Miaojia Guan[a], Bin Zhu[a], Rong Yang[a], Jianrong Qiu[a,*]

[a] State Key Laboratory of Silicon Materials, Zhejiang University, Hangzhou 310027, China
[b] State Key Laboratory of High Field Laser Physics, Shanghai Institute of Optics and Fine Mechanics, Chinese Academy of Science, Shanghai 201800, China
[c] Graduate School of the Chinese Academy of Sciences, Beijing 100039, China

ARTICLE INFO

Article history:
Received 15 July 2010
Received in revised form
28 November 2010
Accepted 30 November 2010
Available online 13 December 2010

Keywords:
Mid-IR emission
Oxyfluoride glass ceramics
Yb^{3+}–Tm^{3+} co-doped

ABSTRACT

Tm^{3+}–Yb^{3+} co-doped transparent oxyfluoride glass ceramics were prepared through thermal treatment of the as-prepared glasses. The precipitation of nanocrystals and the incorporation of Tm^{3+} and Yb^{3+} into the nanocrystals were confirmed by X-ray diffraction and absorption spectra. Based on the Judd–Ofelt theory, the J–O parameters Ω_λ (λ = 2, 4, 6), spontaneous radiative transition rates, radiative lifetimes and fluorescence branching ratios of Tm^{3+} in both as-prepared glasses and glass ceramics were calculated. Intense mid-IR emission and upconversion luminescence in the Tm^{3+} and Yb^{3+} co-doped glass ceramics were observed under 980 nm excitation. Especially, compared with that of the as-prepared glasses, mid-IR luminescence intensity of Tm^{3+} in the glass ceramics was greatly enhanced. Desirable spectroscopic characteristics suggest that these oxyfluoride glass ceramics may be promising mid-IR laser active medium.

1. Introduction

Mid-IR lasers operating in the spectral range of 1.5–2.2 μm have drawn considerable attention for numerous applications, such as eye-safe lasers for radar, remote chemical sensing, military, medicine, and atmospheric monitoring. And a number of different laser systems have been adopted to obtain lasers in the mid-IR range [1]. Lasers utilizing the $^3F_4 \to {}^3H_6$ transition of Tm^{3+} emit coherent photons near 2 μm radiation. And the large degree of Stark Splitting of the $^3H_6$ ground state of Tm^{3+} provides the $^3F_4 \to {}^3H_6$ transition with a very broad emission spanning (400 nm) in many hosts and allows a large degree of wavelength tunability [2]. Therefore, Tm^{3+} activated laser systems have been paid special attention. Lasing operations have been demonstrated at ~2 μm in Tm^{3+} doped crystals [3], silica fibers [4], germanate fibers [5], and tellurite fibers [6].

Silica based oxide glasses generally show better chemical and thermal stabilities than other glass materials. Meanwhile, fluoride crystals are favorable to have good optical properties of rare earth ions. Excellent performance of hybrid materials may be obtained with the combination of the advantages of silica based glasses and fluoride crystals. Fluoride nanocrystals precipitated in the glasses have high solubility of rare earth ions. And high solubility of sensitizer in some degree can improve pump efficiency. Therefore, transparent oxyfluoride glass ceramics, which contain homogeneously distributed fluoride nanocrystals have attracted much attention [7,8]. Efficient neodymium-doped glass–ceramic fiber laser has been reported [9]. And enhanced NIR or mid-IR emission intensities have been demonstrated in Er^{3+}/Yb^{3+} [10,11], and Tm^{3+}/Ho^{3+} [12] co-doped transparent glass ceramics.

Sensitizers are often used for increasing the absorption efficiency of pump light or meeting the wavelength requirements of commercial laser diodes. For Tm^{3+}, Yb^{3+} is a useful co-dopant due to its unique high absorption cross-section and efficient energy transfer to Tm^{3+} ions [13]. In our research, Tm^{3+}/Yb^{3+} co-doped transparent oxyfluoride glass ceramics were fabricated by melt-quenching and subsequent thermal-treatment method. The structural and spectroscopic characteristics of these materials are presented in this paper. According to the Judd–Ofelt theory [14,15], the J–O parameters Ω_λ (λ = 2, 4, 6), spontaneous radiative transition rates, radiative lifetimes and fluorescence branching ratios of rare-earth ions in both as-prepared glasses and glass ceramics were also calculated.

2. Experimental

Oxyfluoride glasses with molar compositions of $60SiO_2$–$20Al_2O_3$–$20CaF_2$–$1TmF_3$–$xYbF_3$ (x = 0, 0.5, 1, 2, 4, 6, 8) were prepared by using high purity (99.99%) SiO_2, Al_2O_3, CaF_2, TmF_3 and YbF_3 as raw materials. The raw materials were mixed and then melted at 1400 °C for 40 min in a covered corundum crucible under atmospheric conditions. The melts were poured onto a cold brass plate and then pressed by another plate. The as-prepared glasses were then heat treated at the first crystallization temperature of the as-prepared glasses (633 °C, determined by the differential thermal analysis (DTA)) for 4 h to obtain transparent glass ceramics. We

* Corresponding author. Tel.: +86 571 88214392; fax: +86 571 88214392.
E-mail address: qjr@zju.edu.cn (J. Qiu).

0925-8388/$ – see front matter
doi:10.1016/j.jallcom.2010.11.192

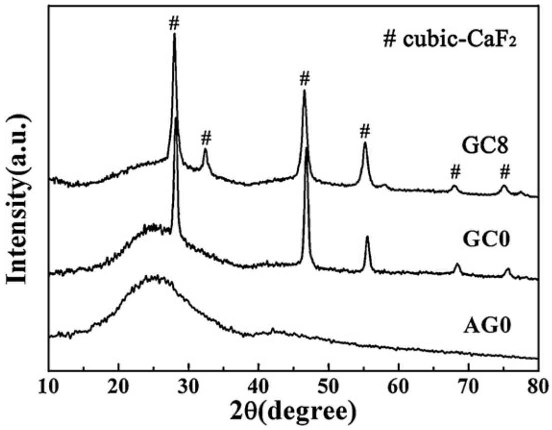

Fig. 1. XRD patterns of samples AG0, GC0 and GC8.

note AG*x* as the as-prepared glass and GC*x* as the glass ceramics, where *x* is the above mentioned molar concentration of YbF_3. The glass and glass ceramic samples were cut and polished to the size of 10 mm × 10 mm × 1 mm for optical measurements.

DTA measurements were carried out in the SDT Q600 differential thermal analyzer in the ambient atmosphere with a heating rate of 5 °C/min to determine the glass transition temperature and the crystallized peak temperature. X-ray diffraction (XRD) measurements were performed on a XD-98 diffractometer with Cu Kα radiation (λ = 1.5418 Å). The microstructures of the samples were observed by JEM-2010 high resolution transmission electron microscopy (HRTEM). Absorption spectra were measured with a JASCO V-570 ultraviolet/visible/infrared spectrophotometer. The emission spectra were measured with an Edinburgh FLS920 fluorescence spectrometer. Meanwhile, a commercial 980 nm laser diode was used as excitation source. All the measurements were carried out at room temperature.

3. Results and discussion

The XRD patterns of AG0, GC0 and GC8 are shown in Fig. 1. The glass sample AG0 is completely amorphous with no sharp diffraction peaks. After crystallization by thermal treatment at 633 °C for 4 h, the XRD patterns of both GC0 and GC8 show intense diffraction peaks, and these XRD patterns can be assigned to cubic CaF_2 phase (JCPDS Card # 77-2093). It can be seen that the XRD peaks of GC8 shift to smaller diffraction angles in comparison to those of GC0, suggesting the occupation of the Ca^{2+} sites by Yb^{3+} or Tm^{3+} ions. By means of Debye–Scherrer's formula, the mean sizes of the precipitated nanocrystals in the GC8 were evaluated to be about 7.4 nm. Fig. 2(a) and (b) shows the TEM and HRTEM images of GC8, respectively. The size of the roughly spherical particles distributed homogeneously in the glass matrix is approximately 6–9 nm, which agrees with the calculated diameter based on Scherrer equation. The diffraction rings of the SAED pattern, as displayed in inset of Fig. 2a, reveal that the nanoparticles are polycrystalline. The large circle can be ascribed to the diffuse scattering of the glassy matrix, and the numerous spots on virtual circles correspond to different diffraction planes.

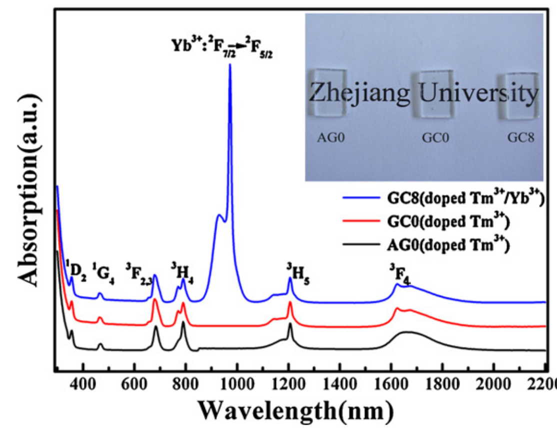

Fig. 3. Absorption spectra of AG0, GC0 and GC8 at room temperature. Some absorption transitions of Yb^{3+} and Tm^{3+} are post-signed. The inset shows optical images of AG0, GC0, and GC8 on top of a printed paper sheet.

Fig. 3 shows the absorption spectra of AG0, GC0 and GC8. The inset clearly shows that the glass and glass ceramics exhibit high transparency. From these absorption spectra, all intrinsic absorption transitions of Tm^{3+} and Yb^{3+} in the region from 300 to 2200 nm are observed. The intensive absorption band near 975 nm wavelength is attributed to the $^2F_{7/2} \rightarrow {}^2F_{5/2}$ transition of Yb^{3+}. It can be seen that after the crystallization process, the absorption bands of the $^3H_6 \rightarrow {}^3H_4$ and $^3H_6 \rightarrow {}^3F_4$ transitions show better resolved Stark components, indicating that the dopant ions have been incorporated into the nanocrystalline phase. Because of the trivalent state of the doping ions, charge compensation has to occur. Different charge compensation mechanisms can occur, leading to different crystal field effects. The inhomogeneous broadening of the absorption spectra is due to site distribution in the unit cell in the nanocrystalline phase [16]. When considering the desirable pumping scheme at 980 nm, a wavelength at which low cost diode lasers are commercially available, the broadening is advantageous since it eliminates the need of temperature control of the diode laser for best tuning conditions.

The Judd–Ofelt (J–O) theory can be used to calculate the optical parameters.

S_{ed} is the line strength for the electric dipole transition between J and J' manifolds, which is given by using following

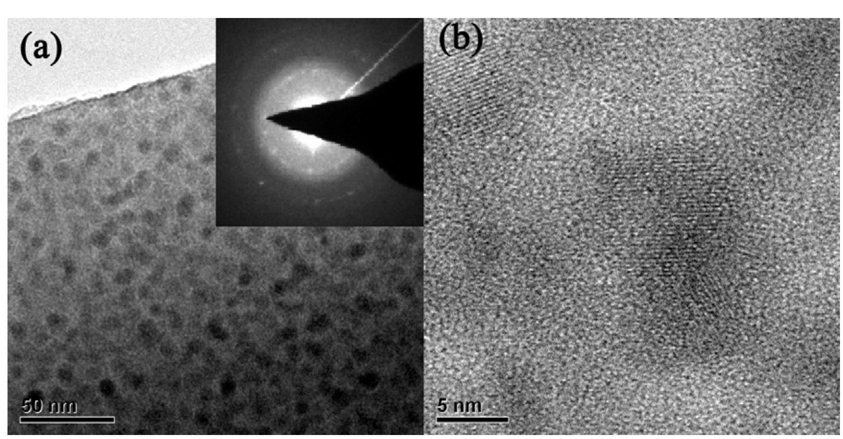

Fig. 2. (a) TEM and (b) HRTEM images of GC8.

Table 1
Calculated optical parameters of Tm^{3+} in AG8 and GC8.

$[SL]J$	$[S'L']J'$	AG8			GC8		
		$A_{JJ'}$ (s^{-1})	$\beta_{JJ'}$	τ_J (ms)	$A_{JJ'}$ (s^{-1})	$\beta_{JJ'}$	τ_J (ms)
$^3F_4$	$^3H_6$	127.225	1	7.860	120.854	1	8.274
$^3H_5$	$^3H_6$	169.212	0.965	5.704	184.887	0.965	5.216
	$^3F_4$	6.10916	0.035		6.8473	0.035	
$^3H_4$	$^3H_6$	666.458	0.873	1.310	671.296	0.873	1.300
	$^3F_4$	73.9493	0.097		73.2223	0.095	
	$^3H_5$	22.82337	0.030		24.79632	0.032	
$^3F_3$	$^3H_6$	987.25	0.834	0.844	1166.74	0.864	0.741
	$^3F_4$	42.9453	0.036		50.8206	0.038	
	$^3H_5$	151.438	0.128		129.326	0.096	
	$^3H_4$	2.82122	0.002		3.04826	0.002	
$^3F_2$	$^3H_6$	232.22	0.404	1.741	278.209	0.468	1.681
	$^3F_4$	242.289	0.422		200.712	0.337	
	$^3H_5$	92.8964	0.162		109.467	0.184	
	$^3H_4$	7.04682	0.012		6.52257	0.011	
	$^3F_3$	0.01877269	0.00003		0.019587	0.00003	
$^1G_4$	$^3H_6$	541.223	0.374	0.691	513.966	0.343	0.668
	$^3F_4$	141.868	0.098		163.442	0.109	
	$^3H_5$	493.466	0.341		540.474	0.361	
	$^3H_4$	187.908	0.130		185.488	0.124	
	$^3F_3$	59.3119	0.041		68.9262	0.046	
	$^3F_2$	22.4635	0.016		25.1505	0.017	
$^1D_2$	$^3H_6$	2616.74	0.224	0.085	3022.48	0.275	0.091
	$^3F_4$	6921.15	0.592		5925.36	0.538	
	$^3H_5$	43.2919	0.004		51.6148	0.005	
	$^3H_4$	749.573	0.064		720.792	0.065	
	$^3F_3$	550.661	0.047		463.009	0.042	
	$^3F_2$	738.378	0.063		763.633	0.069	
	$^1G_4$	71.2182	0.006		63.4434	0.006	

equations [17,18]

$$S_{ed} = \sum_{\lambda=2,4,6} \Omega_\lambda \left| \left\langle S,L,J \right| \left| U^{(\lambda)} \right| \left| S',L',J' \right\rangle \right|, \qquad (1)$$

where Ω_λ (λ = 2, 4, 6) are J–O intensity parameters, $|U^{(\lambda)}|$ is the reduced matrix element, $\left|S,L,J\right\rangle$ and $\left|S',L',J'\right\rangle$ are the energy state. While the magnetic dipole line strength S_{md} is calculated by

$$S_{md} = \left(\frac{h}{2mc}\right)^2 \left| \left\langle S,L,J \right| \left| L+2S \right| \left| S',L',J' \right\rangle \right|^2. \qquad (2)$$

The matrix elements can be calculated by

$$\left| \left\langle S,L,J \right| \left| \mathbf{L}+2\mathbf{S} \right| \left| S',L',J{+}1 \right\rangle \right|^2 = [(S+L+1)^2 - J^2] \left[\frac{J^2-(L-S)^2}{4J}\right] \qquad (3)$$

$$\left| \left\langle S,L,J \right| \left| \mathbf{L}+2\mathbf{S} \right| \left| S',L',J+1 \right\rangle \right|^2 = [(S+L+1)^2 - (J+1)^2] \times \left[\frac{(J+1)^2-(L-S)^2}{4(J+1)}\right], \qquad (4)$$

$\left| \left\langle S,l,J \right| \left| L+2S \right| \left| S',L',J' \right\rangle \right|^2$ is nonzero only if $S = S'$ and $L = L'$.

According to the J–O theory, the theoretical oscillator strength for an electric dipole transition from initial state $\left|S,L,J\right\rangle$ to an excited state $\left|S',L',J'\right\rangle$ is described by

$$F_{theor}^{ED} = \frac{8\pi^2 m\upsilon}{3h(2J+1)} \left[\frac{(n^2+2)^2}{9n}\right] \times \sum_{\lambda=2,4,6} \Omega_\lambda \left| \left\langle S,L,J \right| \left| U^{(\lambda)} \right| \left| S',L',J' \right\rangle \right|^2, \qquad (5)$$

where n is the refractive index of the matrix, m is the mass of the electron, h is the Planck constant, υ is the transition frequency.

From the absorption spectra, experimental oscillator strength of the electronic transition can be calculated by the expression

$$F_{\exp} = \frac{2.303mc^2}{\pi e^2 N d\lambda^2} \int OD(\lambda) d\lambda, \qquad (6)$$

where e is the charge of the electron, c is the speed of the light in vacuum, N is the number concentration of rare-earth ions, d is the thickness of the sample, and $\int OD(\lambda)d\lambda$ is the integrated absorption coefficient.

The spontaneous radiative transition rates A_{rad}, radiative lifetimes τ_J and fluorescence branching ratios β from the excited state $\left|S',L',J'\right\rangle$ to the initial state $\left|S,L,J\right\rangle$ can be calculated from the line strengths. Table 1 presents the calculated results.

$$A_{rad}\left(\left\langle S,L,J | S',L',J' \right\rangle\right) = \frac{64\pi^4 e^2}{3h(2J+1)\lambda^3} \times \left[\frac{n(n^2+1)^2}{9} S_{ED} + n^3 S_{MD}\right], \qquad (7)$$

$$\tau_{rad} = \frac{1}{\sum A_{rad}\left(\left\langle S,L,J | S',L',J' \right\rangle\right)}, \qquad (8)$$

$$\beta \left\langle S,L,J | S',L',J' \right\rangle = \frac{A_{rad}\left(\left\langle S,L,J | S',L',J' \right\rangle\right)}{\sum A_{rad}\left(\left\langle S,L,J | S'',L'',J'' \right\rangle\right)}. \qquad (9)$$

Least-square fitting procedure is applied to calculate Ω_λ (λ = 2, 4, 6) parameters by using the experimentally measured values of oscillator strength for different transitions. Table 2 shows Ω_λ (λ = 2,

Table 2
The J–O parameters of Tm^{3+}-doped AG8 and GC8.

Hosts	Ω_2	Ω_4	Ω_6	Ω_4/Ω_6
AG8	5.76	2.70	2.49	1.09
GC8	4.60	3.69	2.46	1.50

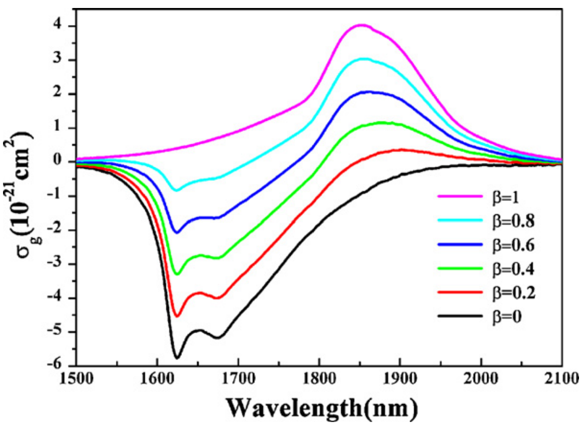

Fig. 4. Calculated gain cross section of $^3F_4 \rightarrow {}^3H_6$ transition of Tm^{3+} in GC8.

4, 6) parameters of Tm^{3+} in AG8 and GC8. It is known that Ω_2 is sensitive to the environment around Tm^{3+} ions, and is associated with the asymmetry and covalency of Tm^{3+} sites. Therefore, the decrease of Ω_2 of Tm^{3+} in GC8 indicates that Tm^{3+} ions have been incorporated into the nanocrystals in the glass ceramic. Besides, $X = \Omega_4/\Omega_6$ is usually regarded as the spectroscopic quality factor [19] and large X value means intense laser transition [14]. The values of X for Tm^{3+} in AG8 and GC8 are 1.09 and 1.50, respectively.

The absorption cross section (σ_{abs}) can be calculated by

$$\sigma_{abs}(\lambda) = 2.303\frac{OD(\lambda)}{Nd}. \tag{10}$$

And the emission cross section (σ_{em}) can be calculated by the expression according to Fuchtbauer–Ladenburg theory [20]

$$\sigma_{em}(\lambda) = \frac{\lambda^4 A_{rad}}{8\pi cn^2} \times \frac{\lambda I(\lambda)}{\int \lambda I(\lambda)\mathrm{d}\lambda} \tag{11}$$

where λ is the wavelength, OD(λ) is the optical density, $I(\lambda)$ is the emission spectrum. The peak absorption and emission cross section of Tm^{3+} in GC8 are 5.07 and 4.01×10^{-21} cm^2, respectively.

The gain cross section (σ_g) at room temperature is obtained by

$$\sigma_g = \beta\sigma_{\text{em}} - (1-\beta)\sigma_{abs}, \tag{12}$$

where $\beta = N_2/N_1$ is the excited state population fraction, N_2 and N_1 are the electron population densities of $^3F_4$ and $^3H_6$ levels of Tm^{3+}, respectively. By assuming a set of β values ranging from 0 to 1, the calculated gain cross section of $^3F_4 \rightarrow {}^3H_6$ transition of Tm^{3+} in GC8 is plotted in Fig. 4. It can be seen that the laser performance wavelengths of the maximum gain cross section shift to longer wavelengths with decreasing the value of β. And this is a typical characteristic of the quasi-three level system.

Fig. 5 presents the room temperature mid-IR emission spectra of Tm^{3+}/Yb^{3+} co-doped AG8 and GC8 under the excitation of 980 nm laser diode. Integrated emission intensities of Tm^{3+} in both as-prepared glasses and glass ceramics as a function of the YbF_3 concentrations are shown in the inset. The mid-IR emission intensities of Tm^{3+} in both glasses and glass ceramics increase monotonically as the concentration of YbF_3 increases from 0 to 8 mol%. Moreover, the integrated emission intensity of Tm^{3+} in glass ceramics increases faster with increasing YbF_3 concentration compared with that of Tm^{3+} in the as-prepared glasses. The relative intensity even increases by two times in glass ceramics under the same excitation condition when YbF_3 concentration is 8 mol%. Due to the reduced distance between the co-dopants in the nanocrystals, an efficient energy transfer may occur between Yb^{3+} and Tm^{3+} after the excitation of Yb^{3+}. This results in a fast depopulation of the excited levels and subsequently feeds the emission band of

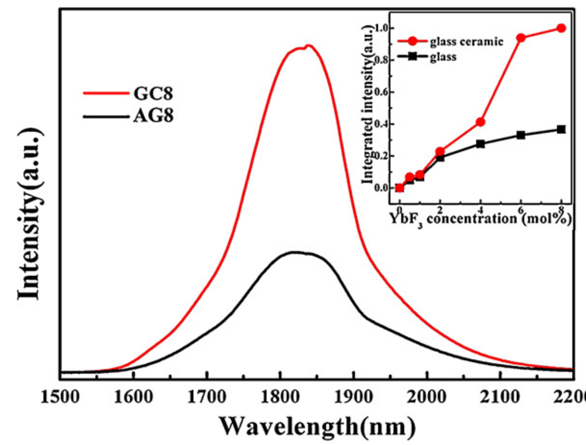

Fig. 5. Mid-IR emission spectra of Tm^{3+} in AG8 and GC8 under 980 nm excitation. The inset shows the integrated mid-IR emission intensities as a function of YbF_3 concentration.

Tm^{3+}: $^3F_4 \rightarrow {}^3H_6$. As the YbF_3 concentration increases, it is advantageous for Yb^{3+} to absorb more pumping light, and Yb^{3+} has only one upper level of $^2F_{5/2}$, which enables Yb^{3+} to easily transfer energy to Tm^{3+}. This is the reason for the increased mid-IR emission intensity. Fig. 6 shows the temperature-dependent luminescence intensity of Tm^{3+}: $^3F_4 \rightarrow {}^3H_6$ in GC8. It is found that the mid-IR emission intensity of Tm^{3+} almost remains constant with increasing temperature. This indicates that the nonradiative relaxation in the GC8 can almost be ignored.

Strong visible emission due to upconversion was also observed in Yb^{3+}–Tm^{3+} co-doped glasses and glass ceramics. This emission was measured to further understand the fluorescence and energy transfer mechanisms. Fig. 7 shows the upconversion emission spectrum in Yb^{3+}–Tm^{3+} co-doped glass ceramics. The emission peaks at approximately 478, 700 and 800 nm can be distinctly assigned to the $^1G_4 \rightarrow {}^3H_6$, $^3F_{2,3} \rightarrow {}^3H_6$, $^3H_4 \rightarrow {}^3H_6$ transitions of Tm^{3+}, respectively. The concentration dependence is illustrated in the inset of Fig. 7. The emission intensities at 478, 700 and 800 nm increase monotonically with an increase in YbF_3 concentration. This could also be ascribed to the enhanced energy transfer rate from Yb^{3+} to Tm^{3+} due to the shortening of the distance between lanthanide ions in the precipitated nanocrystals.

In an upconversion process, the emission intensity (I_{em}) and the excitation power (I_{ex}) of the 980 nm laser diode (LD) have the following relation [21]:

$$I_{\text{em}} \propto (I_{\text{ex}})^n \tag{13}$$

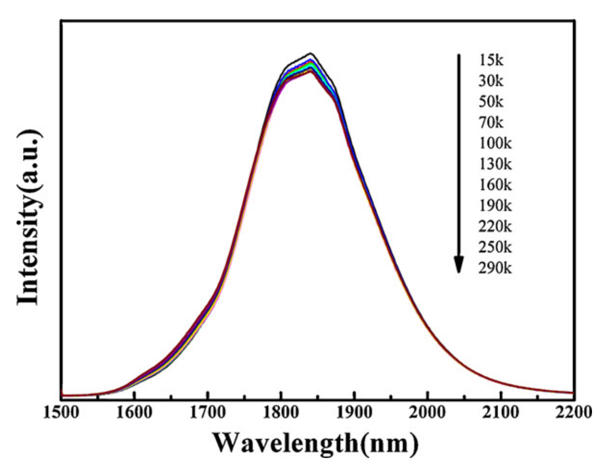

Fig. 6. Temperature-dependent luminescence intensity of Tm^{3+}: $^3F_4 \rightarrow {}^3H_6$ in GC8.

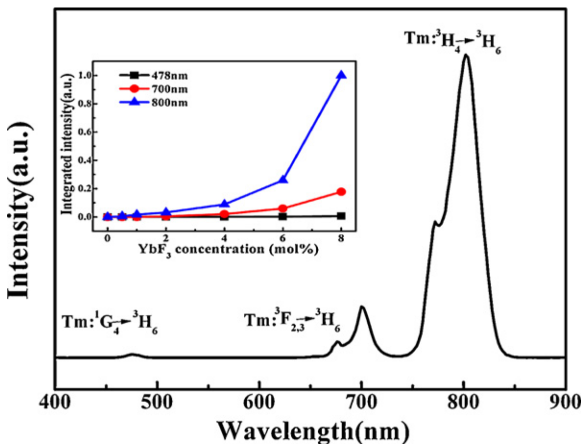

Fig. 7. Visible upconversion luminescence spectrum of Tm^{3+} in GC8 under 980 nm excitation. The inset shows the integrated upconversion luminescence intensities as a function of YbF_3 concentration.

where n represents the number of IR photons needed to populate the visible emitting state. Therefore, a plot of $\log(I_{em})$ versus $\log(I_{ex})$ should yield a straight line with slope n. The dependence of upconversion and mid-IR integrated emission intensities of Tm^{3+} on the LD pump power is shown in Fig. 8. The slope values for the 478, 700, 800 and 1820 nm emission are 2.73, 1.98, 2.20 and 1.18, respectively. The 478 nm-emission signals have an approximately third-power relation with the pump intensity, indicating a three-photon process. Meanwhile, the dependence of the infrared 800 nm fluorescence on pump power is found to be quadratic, thereby indicating a two-photon process. The $^3F_4 \rightarrow {}^3H_6$ transition is related to the one-photon process. Based on these spectroscopic measurements, the possible luminescence mechanisms could be described, as shown in Fig. 9. The Yb^{3+} is excited by a photon and transfers this energy to the Tm^{3+} ion: $^2F_{5/2}$ (Yb^{3+}) + $^3H_6$ $(Tm^{3+}) \rightarrow {}^2F_{7/2}$ (Yb^{3+}) + $^3H_5$ (Tm^{3+}). The Tm^{3+} ion then relaxes from the $^3H_5$ to the $^3F_4$ level and can either decay, emitting at 1820 nm, or absorb another photon, which is called energy transfer (ET): $^2F_{5/2}$ (Yb^{3+}) + $^3F_4$ $(Tm^{3+}) \rightarrow {}^2F_{7/2}$ (Yb^{3+}) + $^3F_{2,3}$ (Tm^{3+}) or excited-state absorption (ESA): $^3F_4$ (Tm^{3+}) + a photon → $^3F_{2,3}$ (Tm^{3+}). The Tm^{3+} ion at the $^3F_{2,3}$ level can do one of the following three things: decay, emitting at 700 nm, nonradiatively relax (NR) from the $^3F_{2,3}$ to the $^3H_4$ level, decay, emitting at 800 nm or absorb yet another photon: ET: $^2F_{5/2}$ (Yb^{3+}) + $^3H_4$ $(Tm^{3+}) \rightarrow {}^2F_{7/2}$ (Yb^{3+}) + $^1G_4$ (Tm^{3+}) or ESA: $^3H_4$ (Tm^{3+}) + a photon → $^1G_4$ (Tm^{3+}). In this latter case, the Tm^{3+} ion decays from the $^1G_4$ level and emits at 478 nm.

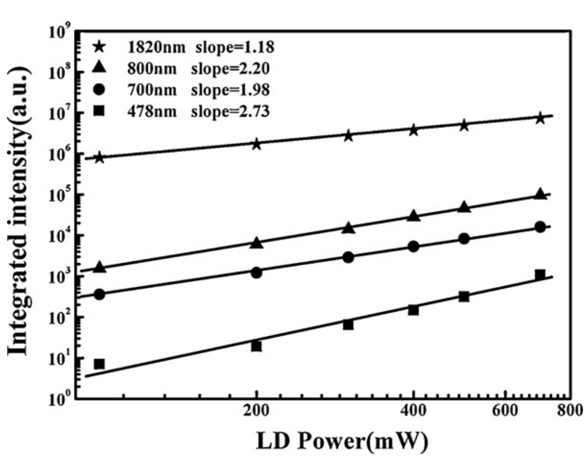

Fig. 8. Dependence of upconversion and mid-IR integrated emission intensities of Tm^{3+} in GC8 on LD pump power.

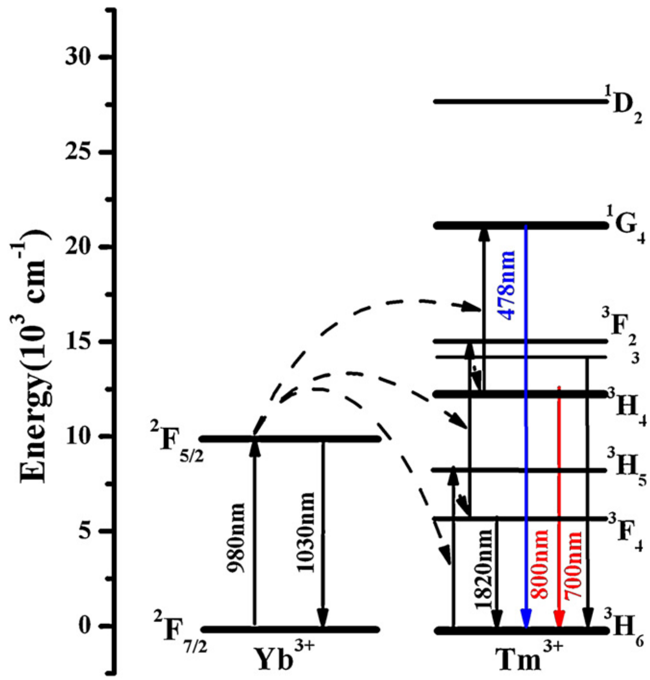

Fig. 9. Simplified energy levels diagram of Tm^{3+} and Yb^{3+} ions and possible luminescence mechanisms.

4. Conclusions

In summary, Tm^{3+} and Yb^{3+} co-doped transparent oxyfluoride glasses and glass ceramics were prepared and characterized. The J–O parameters, spontaneous radiative transition rates, radiative lifetimes and fluorescence branching ratios of Tm^{3+} in both as-prepared glasses and glass ceramics were obtained according to Judd–Ofelt theory. The XRD results, absorption spectra and optical parameters suggested that Tm^{3+} and Yb^{3+} ions had been enriched in the nanocrystals of the glass ceramics. Due to reduced distance between lanthanide ions in the precipitated fluoride nanocrystals, mid-IR emission intensity of Tm^{3+}/Yb^{3+} co-doped glass ceramics was found to be stronger than that of Tm^{3+}/Yb^{3+} co-doped glasses as a result of enhanced energy transfer rate from Yb^{3+} to Tm^{3+}. This ET also contributed to the observed strong visible upconversion emissions of Tm^{3+} located at 478, 700 and 800 nm for the glass ceramic samples. The results show the potential application of Tm^{3+}/Yb^{3+} co-doped oxyfluoride glass ceramics as mid-IR tunable laser/amplifier media.

Acknowledgements

This work was financially supported by the National Natural Science Foundation of China (grant nos. 50672087, 50872123 and 50802083), the National Basic Research Program of China (2006CB806000b), and the Program for Changjiang Scholars and Innovative Research Team in University (IRT0651).

References

[1] A. Godard, C. R. Phys. 8 (2007) 1100–1128.
[2] D.C. Hanna, R.M. Percival, R.G. Smart, A.C. Tropper, Opt. Commun. 75 (1990) 283–286.
[3] G. Galzerano, F. Cornacchia, D. Parisi, A. Toncelli, M. Tonelli, Opt. Lett. 30 (2005) 854–856.
[4] Y.H. Tsang, D.J. Coleman, T.A. King, Opt. Commun. 231 (2004) 357–364.
[5] J.F. Wu, S.B. Jiang, T. Luo, J.H. Geng, N. Peyghambarian, N.P. Barnes, IEEE Photonics Technol. Lett. 18 (2006) 334–336.
[6] B. Richards, Y. Tsang, D. Binks, J. Lousteau, A. Jha, Opt. Lett. 33 (2008) 402–404.
[7] H. Ping, D.Q. Chen, Y.L. Yu, Y.S. Wang, J. Alloys Compd. 490 (2010) 74–77.

[8] S.F. Leon-Luis, J. Abreu-Afonso, J. Pena-Martinez, J. Mendez-Ramos, A.C. Yanes, J. del-Castillo, V.D. Rodriguez, J. Alloys Compd. 479 (2009) 557–560.
[9] B.N. Samson, P.A. Tick, N.F. Borrelli, Opt. Lett. 26 (2001) 145–147.
[10] X.C. Yu, F. Song, W.T. Wang, L.J. Luo, L. Han, Z.Z. Cheng, T.Q. Sun, J.G. Tian, E.Y.B. Pun, J. Appl. Phys. 104 (2008).
[11] G. Dantelle, M. Mortier, D. Vivien, G. Patriarche, Chem. Mater. 17 (2005) 2216–2222.
[12] W.J. Zhang, Q.Y. Zhang, Q.J. Chen, Q. Qian, Z.M. Yang, J.R. Qiu, P. Huang, Y.S. Wang, Opt. Expr. 17 (2009) 20952–20958.
[13] F. Auzel, Chem. Rev. 104 (2004) 139–173.
[14] L.V.G. Tarelho, L. Gomes, I.M. Ranieri, Phys. Rev. B 56 (1997) 14344–14351.
[15] V.K. Tikhomirov, J. Mendez-Ramos, V.D. Rodriguez, D. Furniss, A.B. Seddon, J. Alloys Compd. 436 (2007) 216–220.
[16] G. Dantelle, M. Mortier, D. Vivien, Phys. Chem. Chem. Phys. 9 (2007) 5591–5598.
[17] Q. Zhang, G.R. Chen, G. Zhang, J.R. Qiu, D.P. Chen, J. Appl. Phys. 107 (2010).
[18] F. Liu, E. Ma, D.Q. Chen, Y.S. Wang, Y.L. Yu, P. Huang, J. Alloys Compd. 467 (2009) 317–321.
[19] D.K. Sardar, J.B. Gruber, B. Zandi, J.A. Hutchinson, C.W. Trussell, J. Appl. Phys. 93 (2003) 2041–2046.
[20] A. Kermaoui, F. Pelle, J. Alloys Compd. 469 (2009) 601–608.
[21] D.M. Shi, Q.Y. Zhang, G.F. Yang, C. Zhao, Z.M. Yang, Z.H. Jiang, J. Alloys Compd. 466 (2008) 373–376.